Contents lists available at ScienceDirect

Earth and Planetary Science Letters

journal homepage: www.elsevier.com/locate/epsl

Kilometer-wide crustal yielding associated with the 2021 M_w7.4 Maduo, Tibet, surface rupture

S.L. Antoine [1,a,b,*], Z. Liu [a], R. Mallick [a,c], A. Delorme [b], Y. Klinger [b]

[a] NASA Jet Propulsion Laboratory, California Institute of Technology, Pasadena, CA, USA
[b] Université de Paris Cité, Institut de physique du globe de Paris, CNRS, F-75005 Paris, France
[c] Earth Observatory of Singapore, Nanyang Technological University, Singapore

ARTICLE INFO

Editor: Dr H Thybo

Keywords:
High-resolution optical image correlation
Maduo
Surface displacement
Diffuse deformation
Yielding
Buried rupture
Shallow slip deficit
Strike-slip earthquake

ABSTRACT

When rupturing the surface, earthquakes can generate large-scale permanent deformation up to significant distance of the main ground rupture, referred to as off-fault deformation (OFD). Part of this deformation localizes along secondary ruptures, while some part is diffuse in the medium. The contribution of the diffuse OFD to the rupture process and long-term deformation budget, as well as its underlying physical mechanisms are however not fully understood. The 2021/05/21 M_w7.4 Maduo, Tibet, strike-slip earthquake generated discontinuous surface rupture along a curvilinear fault, associated with extensive OFD. It represents a good case to study the relations between rupture process and localization of the surface deformation because of the limited influence of confounding factors such as geometrical complexity from cross-cutting faults. We compute high-resolution near-fault displacement maps from optical image correlations for this event, and measure the contributions of on- and off-fault deformation along the ~160 km-long rupture area. Majority of the surface coseismic deformation is accommodated by OFD, especially in the epicentral area where no surface slip was observed and the deformation appears as diffuse over a ~1.5 km wide area. Displacement gradients across the diffuse deformation regions, representing a first order approximation of the accommodated strain, are dominantly below 0.3%. Using two-dimensional mechanical models, we investigate whether such diffuse surface deformation includes an inelastic component as it would have critical implications for the determination of the earthquake energy budget, and the fault zone displacement budget over the seismic cycle. Our results show that yielding could account for part of the diffuse deformation, then accounting for the deficit in shallow fault slip in the regions of surface rupture gap.

1. Introduction

Understanding the mechanisms and controlling parameters of the surface deformation associated with continental earthquake ruptures is key to our understanding of earthquake and faulting processes, especially in the shallow crust where rocks and faults present diverse mechanical behaviors due to the lower temperature and pressure conditions, and the presence of less consolidated materials (Byerlee, 1978; Scholz, 1998). Assessing the budget of elastic, i.e. reversible, and inelastic, i.e. irreversible, deformation in the shallow crust (Antoine et al., 2021; Nevitt et al., 2020) is then necessary to determining the total earthquake energy budget (Okubo et al., 2019), as well as the fault zone displacement budget and structural evolution over geologic times (Zinke et al., 2015; Perrin et al., 2016). In the case of an isolated locked fault in an elastic medium, elastic deformation is a process by which elastic strain energy builds up in between earthquakes and is released during an earthquake (Reid, 1911). Creeping faults, on the other hand, release elastic strain continuously during the inter-seismic period through aseismic slip (e.g., Jolivet et al., 2012; Li et al., 2021). Observation of aseismic slip on a fault at a certain time however does not preclude this fault from hosting earthquakes (Chen and Bürgmann, 2017; Harris, 2017). In all these configurations, the long-term strain budget is fully accounted for by slip on the fault.

However, for most continental earthquake ruptures, the amount of slip measured along the faults at the surface is lower than that suggested to occur at depth in slip models (Antoine et al., 2024; Sethanant et al., 2023). It has been shown that shallow afterslip, aftershocks, or creep following those events are not large enough that they would account for

* Corresponding author.
E-mail address: solene.antoine@hotmail.fr (S.L. Antoine).
[1] Now at Division of Geological and Planetary Sciences, California Institute of Technology, Pasadena, California, USA

https://doi.org/10.1016/j.epsl.2026.119868
Received 24 April 2025; Received in revised form 16 January 2026; Accepted 20 January 2026

this difference (Jin et al., 2023; Pousse-Beltran et al., 2020). This observation calls for other processes than fault slip to accommodate strain in the shallow crust, with macroscopic yielding proposed as a potential candidate (Fialko et al., 2005; Jin et al., 2023; Kaneko and Fialko, 2011; Nevitt et al., 2020). Yielding occurs at the transition between linear elasticity and localized failure of the material (McBeck et al., 2021). While the exact functional form for yielding is not well known, the yield criterion can be defined through a combination of brittle, elasto-plastic, and sometimes viscous mechanisms (Nicolas et al., 2017; Petit et al., 2024). It can occur during the earthquake rupture, as part of the dynamically triggered off-fault damage (Okubo et al., 2019), but also in regions of lesser or no fault slip, especially in the shallow crust where elasto-visco-plastic processes accommodate part of the accumulated strain (Mia et al., 2023; Nevitt et al., 2020). Then, the long-term strain budget is partitioned between slip on the primary fault, and non-elastic deformation of the surrounding medium.

Focusing on the coseismic period, surface deformation can be described as a combination of localized deformation on faults, off-fault inelastic deformation (OFD; Antoine et al., 2021, 2022; Milliner et al., 2016), and elastic response of the surrounding so called "intact" medium (Kanamori and Brodsky, 2004). OFD has been generally characterized to be a few tens to a few hundreds of meters wide (e.g., Milliner et al., 2016; Zinke et al., 2019); however, wider ($>$ 1 km) and more continuous surface deformation, sometimes referred to as diffuse deformation, can also be considered as part of the OFD (e.g., Antoine et al., 2022, 2021; C. Li et al., 2022; Liu et al., 2025; Provost et al., 2024; Xi et al., 2025). Although, it is highly debated whether such wide diffuse surface deformation should be considered as part of the inelastic or elastic deformation budget. Considering the diffuse deformation as involving an inelastic component would then question the validity of the pure-elastic assumption used in earthquake rupture models, especially in the shallow near-fault domain (Mia et al., 2023; Nevitt et al., 2020). It would also question the accuracy of fault energy budget estimate using geological slip rate and historical earthquake records derived from offset landforms and paleoseismic observations given that part of the long-term strain budget could be accommodated off the faults (Reitman et al., 2022; Shelef and Oskin, 2010), especially for immature faults (Zinke et al., 2015). Off-fault inelastic deformation also affects the mechanical behavior of the medium, and so the faults' mechanical and seismic behavior (Abdelmeguid and Elbanna, 2022). These modifications have an impact on the rupture process at the scale of an individual earthquake (e.g., Idini and Ampuero, 2020), as well as over multiple seismic cycles (e.g., Perrin et al., 2016; Thakur and Huang, 2021).

Considering the 2021 Maduo earthquake rupture, this study aims at characterizing the patterns of on- and off-fault deformation, and their respective spatial distribution, to propose plausible deformation mechanisms for the diffuse off-fault deformation. Using high-resolution optical image correlation (OIC), we produce near-fault displacement maps, measure the on- and off-fault displacement budget, and derive the displacement gradients of the on- and off-fault deformation as a first order estimate of the surface strain accommodated across the different regions. Using simple mechanical models, we assess the possibility for the diffuse strain along different regions of the 2021 Maduo rupture to include an inelastic component.

2. The 2021 M_w7.4 Maduo, Tibet, rupture

The 2021 Maduo earthquake ruptured a ~160 km-long portion of the left-lateral strike-slip Jiangcuo fault, within the Bayan Har block of the Eastern Tibetan plateau, at about 100 km South of the Kunlun fault (He et al., 2021; J. Ren et al., 2022). The geometry and slip rate of the Jiangcuo fault are poorly known. However, paleoseismic studies suggest a slip rate of 0.35–0.55 mm/yr (Pan et al., 2022; J. Ren et al., 2022). Analysis of geomorphic offsets showed a possible cumulative fault displacement of ~4–5 km, decreasing towards the SE (C. Li et al., 2022). On May 21, 2021, the rupture nucleated at a depth of ~10–17 km, and propagated bilaterally (Fan et al., 2022; Liu et al., 2022; Wei et al., 2022). Published earthquake rupture models suggest a maximum slip of ~5–6 m located at ~3–5 km depth, mostly dominated by left-lateral displacement (e.g., He et al., 2021; Jin and Fialko, 2021; Wei et al., 2022). Despite its magnitude, the surface rupture associated with the 2021 Maduo event is very discontinuous, and surface deformation occurred for a large part on distributed fractures (e.g., Han et al., 2024; Liu-Zeng et al., 2024; J. Ren et al., 2022, J. 2021; Yuan et al., 2022). Continuous surface ruptures are primarily reported along the NW and SE extremities of the rupture, while they are separated by two major rupture gaps in the central part. Field studies reported primarily horizontal offsets, with a dominant range between 0.5 and 1.5 m, and maximum local values up to 2.6–2.9 m (Pan et al., 2022; J. Ren et al., 2022; J. 2021; Xie et al., 2022; Yuan et al., 2022). When averaged along the 160-km length of the 2021 Maduo rupture, average left-lateral surface displacement is 0.4 m from field observations (Yuan et al., 2022), and ~2–3 m from geodetic measurements (Jin and Fialko, 2021; C. Li et al., 2022). This difference is interpreted as resulting from large OFD along the Maduo rupture (C. Li et al., 2022). Overall, the Maduo earthquake presents heterogeneous surface deformation characterized by along-strike transitions from localized to diffuse deformation making this earthquake a good example to analyze the mechanisms and controls of the surface deformation localization.

3. Material and methods

3.1. Data and method of the optical image correlation

We use high-resolution OIC to capture near-fault surface displacements associated with the 2021 Maduo rupture. Data include high-resolution stereo and tri-stereo pre-earthquake SPOT6–7 (1.6 m Ground Sampling Distance, GSD) and post-earthquake Pleiades (0.5 m GSD) satellite optical images (Tab. S1). In total, fourteen combinations of pre- and post-earthquake images were used to cover the 160 km-long study area from East to West (Fig. S1). All data are downloaded on a High-Performance Computer, and processed using the MicMac photogrammetry and OIC software (Rosu et al., 2015; Rupnik et al., 2018), along with Python, MATLAB, and GDAL for the pre- and post-processing. Pleiades data cover only a $\pm$ 5 km-wide swath along the 2021 Maduo rupture trace (Figs. 1a, 1b, and S1). Hence, the calculations are performed only within this area. Even though SPOT6/7 pre-earthquake images have a 1.6 m GSD, all processing steps are performed at a 0.5 m GSD, which is the native GSD of the Pleiades images. Impact of the resampling and choice of the common GSD (between 0.5 and 1.6 m) have been tested, and the 0.5 m GSD results show lower background noise (Fig. S2).

(Tri-)stereo images from both the pre- and post-earthquake periods are used to calculate respectively pre- and post-earthquake Digital Surface Models (DSM). The DSMs are used to orthorectify (correct from viewing angle and topography distortions, and project in a common ground reference; Leprince et al., 2007; Rupnik et al., 2018) the pre- and post-earthquake optical images, respectively. Using DSMs directly computed from the same images later used for OIC reduces possible orthorectification bias due to the use of low-resolution topography models, and georeferencing errors (Antoine and Liu, 2025). In addition, the use of distinct pre- and post-earthquake DSMs to orthorectify images acquired before and after the earthquake avoids introducing errors related to change in the topography during the earthquake (Antoine and Liu, 2025). Pairs of pre- and post-earthquake orthorectified images are then cropped to their common areas for OIC purposes. OIC is performed using a correlation window of 5 pixels (2.5 m) in all iterations, a sub-pixel correlation step of 1/20th of a pixel, and a spatial regularization based on a displacement continuity constraint of 0.3. These parameters are uniform across the processed images tiles, and no adjustment of the correlation window is made during processing, for example with the coherence or gradient of the measured displacements.

The search space is set to 5 m for most image pairs, but increased to 7 m for a few pairs that recorded geomorphic and meteorological activity of amplitudes above that of the earthquake-related displacements. Taking advantage of the two to three available images for the pre- and post-earthquake periods, we performed OIC for all the possible pairs straddling the earthquake date, and stacked the results that present the least artifacts. Stacking operation is performed using a weighted average method based on the correlation score map outputs of the OIC process, allowing for an increase of the signal to noise ratio (Delorme et al., 2020). The final stacked OIC results obtained for different sub-areas are corrected for ramp artifacts (usually from camera bundle block adjustment residuals; e.g., Fig. S3) using lower-resolution SAR-derived horizontal displacement maps from Liu et al. (2022) that provide a common reference. A polynomial function is fit to the difference between SAR and OIC at low frequency, and removed from the OIC results (Fig. S3a-e). Sentinel-2B OIC was also performed to cross-check the quality of the ramp corrections, and validate our method of ramp removal using SAR results (Tab. S2, and Figs. S3f and S4). Overall, this method preserves the high-frequency signal that corresponds to the coseismic deformation, along with some other local artifacts (decorrelation in regions with clouds, or affected by sedimentary transport such as drainages, wetlands and dune fields; Fig. 1a). Through specific shape and/or direct visual identification in the optical images, we identified the local artifacts and ignored them when performing the earthquake-related displacements analysis.

Finally, we tested the possibility of measuring the vertical displacements from differencing the elevation between the pre- and the post-earthquake DSMs whose features have been horizontally realigned using the horizontal displacements measured previously (Antoine et al., 2022, 2021; Delorme et al., 2020). However, uncertainty in the resulting products reaches an amplitude of ±1 m, which prevents any systematic analysis of the vertical deformation (Fig. S5; Antoine and Liu, 2025). Thus, from here, our work focuses only on the horizontal components of the surface displacement.

3.2. Across-fault displacement measurements from the OIC results

We use stacked profiles to analyze how the fault-parallel surface displacements distribute between localized deformation on faults, and OFD along the 2021 Maduo surface rupture. Stack boxes are placed every 200 m along the ~160 km-long 2021 Maduo rupture, including the diffuse deformation regions, for a total of 781 cross-fault profiles. Profile length ranges from 1 to 5 km, allowing to capture the entire deformation across the fault zone, even in regions of large, >1.5 km, diffuse deformation. Within each 200 m-wide boxes, displacements are stacked using a weighted median method based on the output OIC correlation score. Fault-parallel displacements are derived from the combination of the E-W and N-S displacements along the stack profile with respect to the local fault azimuth (StackProf software; See Open Research statement).

Total surface displacement across each profile is assessed by measuring the offset between the best fitting linear regressions of the displacements outside of the fault zone (horizontal black dashed lines in Fig. 2c). Localized deformation on faults is identified from the sub-vertical offsets in the displacement profiles (e.g., in profiles AA' and CC' in Fig. 2c). This measurement is cross-checked using the detailed field rupture maps available for this earthquake (black lines in Fig. 2a) that highlight the presence of primary faults in the localized deformation regions we identified. In the example of profile CC' (Fig. 2), two ruptures were mapped in the field, though we detected only one offset showing that the second rupture located northward did not accommodate enough slip to reach our detection threshold, of ~16 cm given the resolution of 1.6 m of the SPOT6-7 images. OFD for each profile is then derived from the difference between the total displacement and the localized deformation offsets. Similar approaches have been commonly used to characterize earthquake surface deformation based on OIC results, although profile widths and lengths can vary (e.g., Antoine et al., 2021, 2022; Gold et al., 2015; C. Li et al., 2022; Milliner et al., 2016; Scott et al., 2018). Since the total displacement is also measured across the diffuse deformation regions, diffuse deformation is included in the surface displacement budget as OFD.

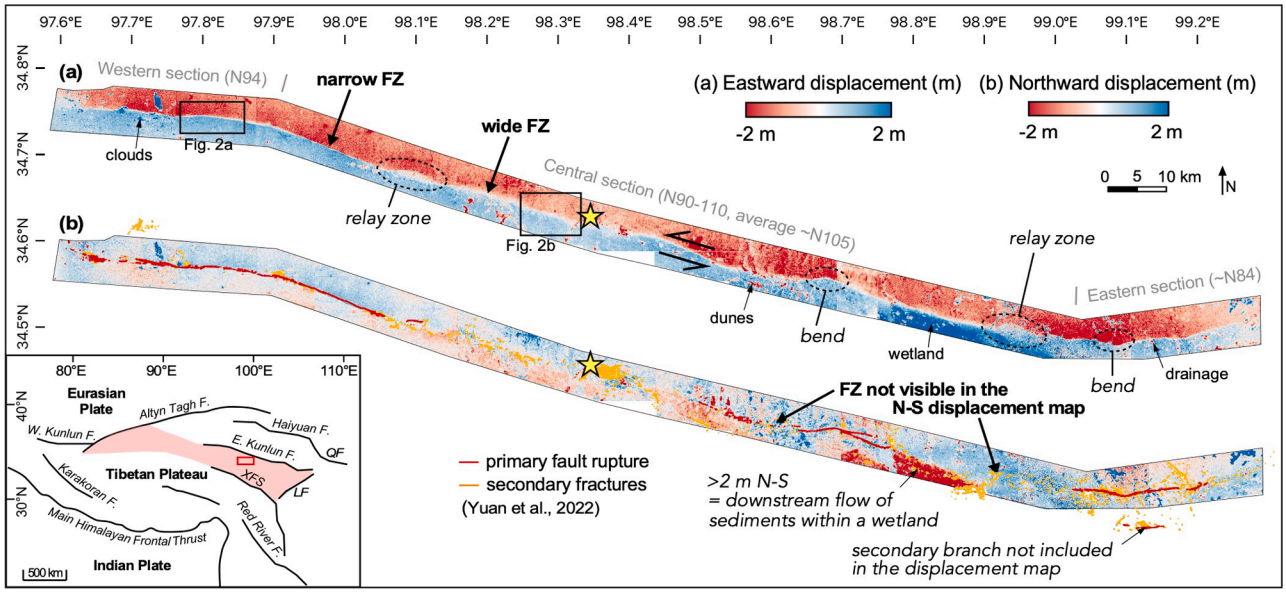

Fig. 1. (a) East-west (E-W) and (b) north-south (N-S) surface displacements along the 2021 Maduo rupture from optical image correlation. The rupture area appears as a continuous and curvilinear structure separating the N-E and the S-W blocks. Some geometrical complexities, including bends and relay zones, are indicated using dashed-line circles. Examples of artifacts related to geomorphic or meteorologic processes are highlighted with thin black arrows. Epicenter location, from global CMT catalog (GCMT), is shown with a yellow star. Field rupture map from Yuan et al., 2022 is overlaid in (b) with, in red, the primary ruptures, and in orange, the secondary fractures. Inset at the bottom left shows the tectonic context, modified from J. Ren et al. (2022). Light red area is the Bayan Har block. Red box is the area of (a). LF is the Longmenshan Fault. XFS is the Xianshuihe Fault System. QF is the Qinling Fault.

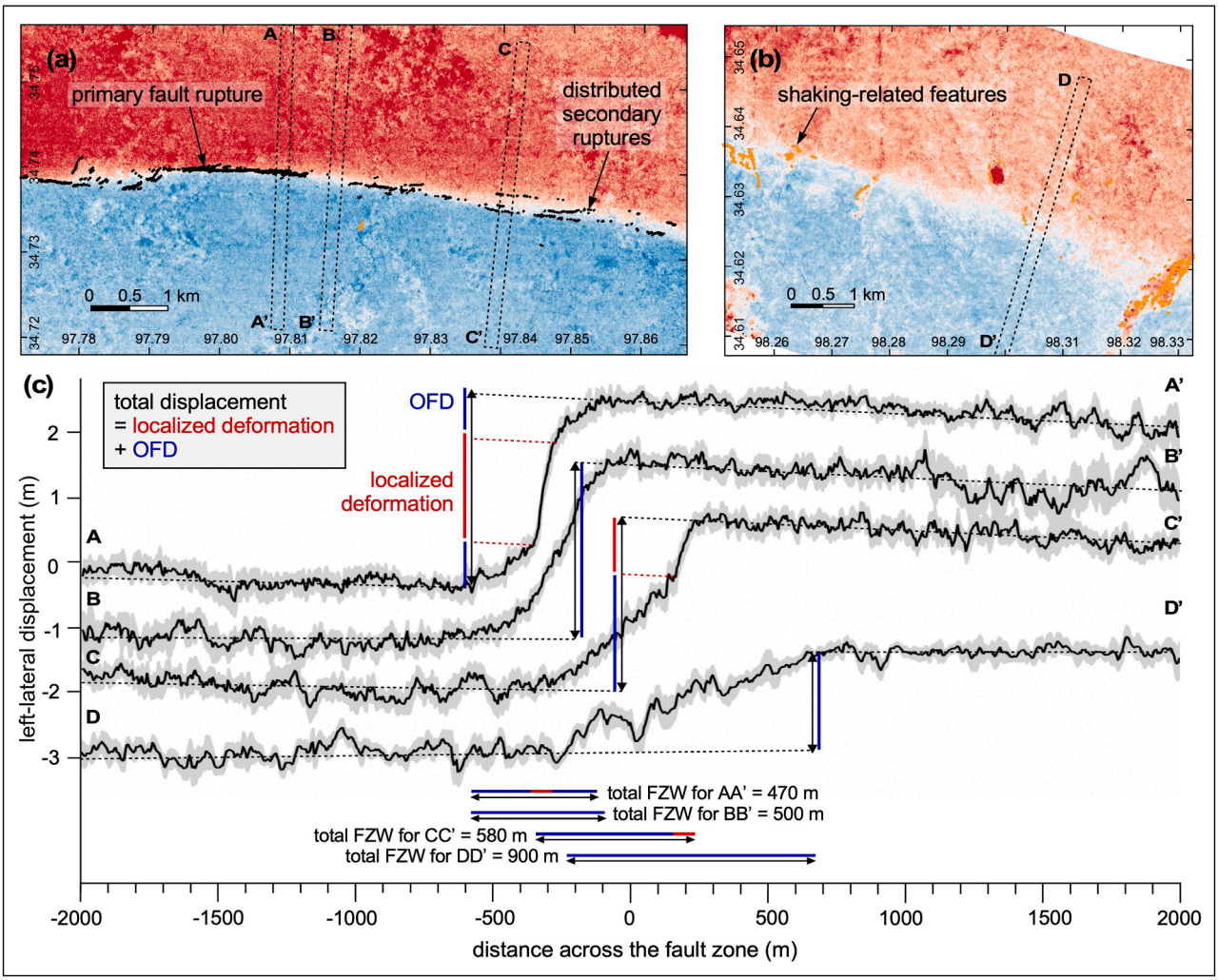

Fig. 2. Zoom in the E-W displacement map from Fig. 1 in (a) a region with primary fault ruptures, and (b) a region of diffuse deformation. Rupture map is from Yuan et al. (2022). Dashed boxes are displacement profiles displayed in (c). (c) Fault-parallel displacement profiles across (a) and (b). Dashed black lines are linear regressions used to measure the total displacement, reported using vertical black arrows. Red dashed lines highlight the separation between regions of localized deformation (red) and OFD (blue). Colored vertical bars report the respective contributions of each deformation mode to the total displacement. Below the profiles are reported horizontally the total FZW (black arrow) and the respective width of the localized and OFD zones (colored bars). These widths are measured from the horizontal extension of, respectively, the total displacement, and localized deformation and OFD zones.

3.3. Modeling of the deformation

We use a forward two-dimensional (2D) Boundary Element Method (BEM) to model bulk stress change, and therefore estimate the possibility for bulk inelastic deformation given some assumptions on the bulk mechanical characteristics and buried fault slip distribution. We did not attempt inverting for fault slip using the optical observations since it is not the primary goal of this study, and that finite slip models have already been proposed in other studies (e.g., Jin and Fialko, 2021; Tong et al., 2022; Xiong et al., 2022; L. Zhao et al., 2023). We specifically use the slip distribution of Zhao et al. (2023a) who inverted surface displacements measured from Sentinel-2 optical image correlation to inferr the shallow slip distribution of the 2021 Maduo rupture. We also test endmember models including a deeply buried rupture, and a throughgoing rupture with maximum slip at the surface.

The BEM approach allows computing displacements and stresses in an elastic medium subjected to the following boundary conditions: i) imposed slip on the fault, and ii) traction-free conditions on the free surface (Mallick and Meade, 2025; Fig. S6). The method only requires discretizing the fault geometry and surface topography profile while deformation within the bulk can be predicted without meshing. From the modeled stress tensor, we predict the macroscopic Criterion for Failure (CF) using a Mohr-Coulomb type of failure threshold that estimates the bulk yield stress (τ_f), that is the stress at which the bulk medium starts to deform in an irreversible manner, as a function of depth:

$$\tau_f = c + f \times \sigma_n \quad (1)$$

with c the cohesion, f the friction coefficient, and σ_n the normal stress (King et al., 1994). There are not existing constraints on the amplitude of absolute stresses in the medium, therefore we consider the normal stress to be equivalent to a depth-dependent pressure term defined as follow:

$$P_z = \Delta\rho \times g \times z \quad (2)$$

with $\Delta\rho$ the effective bulk density which equals to the crustal density minus the density of water, g the gravity, and z the depth (Jaeger et al., 2007). Near-surface effects can lead to variations in the fault-normal stresses (Jaeger et al., 2007; Moon et al., 2020), introducing an additional component of fault strength which is absorbed within the range of cohesion and friction coefficient values tested. We also consider the general case of a vertical fault, which is close to the actual geometry of the Jiangcuo fault in the epicentral area (84–90°N ; Fan et al., 2022;

Wang et al., 2021).

CF then corresponds to the ratio between the modeled stress change across the bulk medium ($\Delta\sigma$), and the bulk shear strength estimated from Eq. (1):

$$CF = \frac{\Delta\sigma}{\tau_f} \tag{3}$$

In this study, we first assess the shear modulus and depth ranges favorable to bulk yielding, and then present the 2D models of bulk CF for the proposed slip distributions. We eventually test the sensitivity of the 2D CF models to bulk shear modulus, friction and cohesion in Figure S7b-d.

4. Results

4.1. Horizontal surface displacement maps

Horizontal surface displacements measured from OIC along the 2021

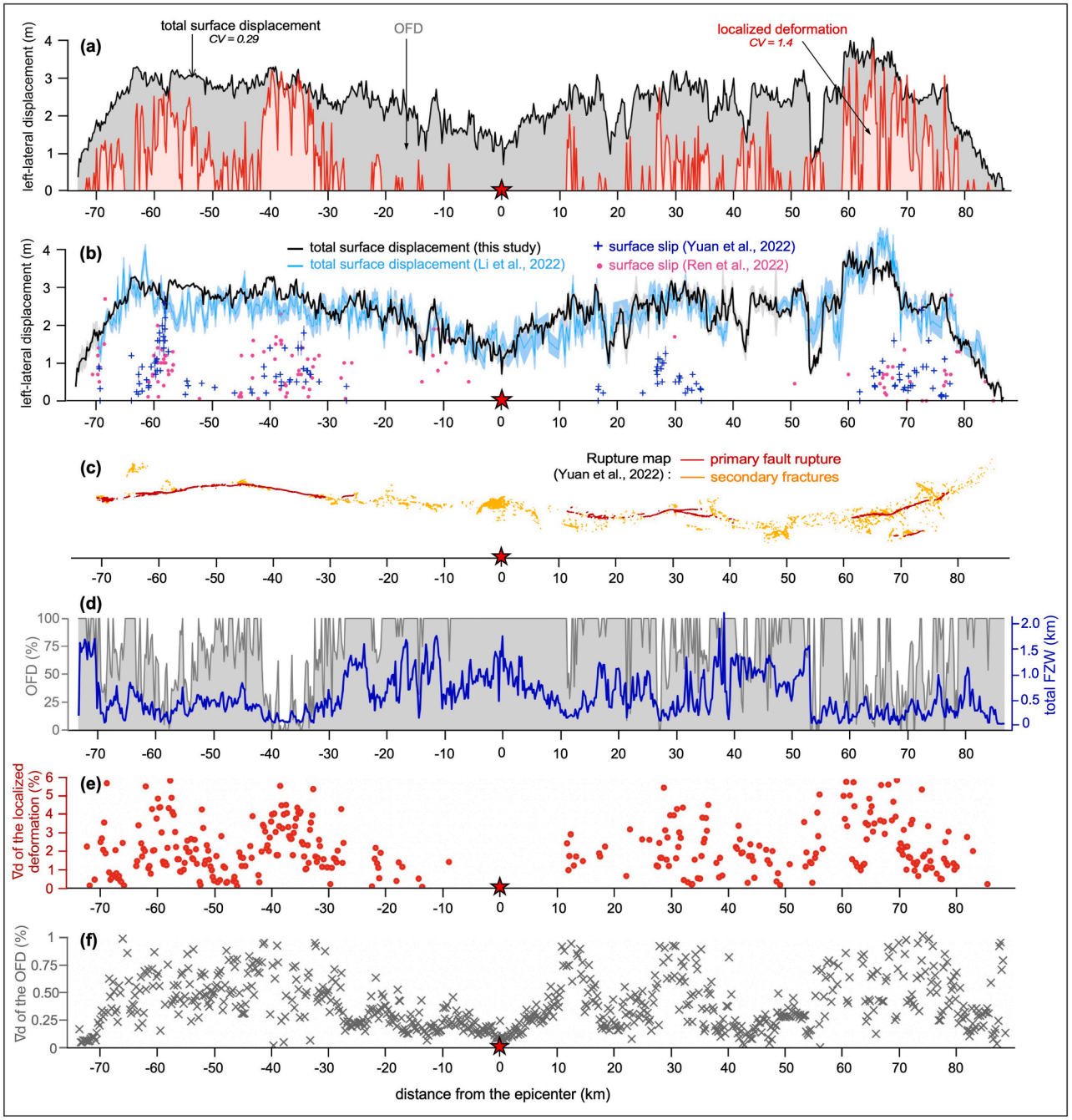

Fig. 3. (a) Surface displacement budget of the 2021 Maduo rupture (top plot). Black curve is the total surface displacement. Red curve is the localized deformation. Grey area is the OFD. The coefficients of variation (CV; ratio between the standard deviation and the mean) reflect the degrees of variability of each curve. (b) Comparison between total displacements measured from optical OIC (curves; this study and C. Li et al., 2022) and faults offsets measured in the field (points and crosses; Yuan et al. 2022, and J. Ren et al., 2022), in the left-lateral component. (c) Field map of the 2021 Maduo surface rupture including, in red, the primary faults, and in orange, the secondary fractures (Yuan et al., 2022). (d) Evolution of OFD, in percents (grey curve), and Fault Zone Width (FZW) along the rupture strike. (e) Displacement gradients $\nabla \boldsymbol{d}$ measured across the localized deformation regions. (e) Displacement gradients $\nabla \boldsymbol{d}$ measured across the OFD regions. Scatter in (e) and (f) arise from measurement variability amplified when deriving the gradients.

Maduo earthquake show a dominant east-west (E-W) component (Fig. 1a), together with a minor north-south (N-S) component (Fig. 1b) that is only detectable at a few locations, when excluding artifacts due to sediment movements along rivers, wetlands, and dunes. This is consistent with the left-lateral strike-slip motion determined from seismological and geodetic data (e.g., Fan et al., 2022; He et al., 2021; Jin and Fialko, 2021; C. Li et al., 2022), and field observation (Liu-Zeng et al., 2024; Pan et al., 2022; J. Ren et al., 2022; Xie et al., 2022; Yuan et al., 2022). The Maduo rupture zone is visible in the OIC results as the transition region between red to blue colors, that respectively represent the displacement of the blocs north and south of the rupture zone. The geometry of this rupture zone is consistent with the field rupture maps (Figs. 1b, 2a,b). Rupture azimuth variations associated with local geometrical asperities are found all along the Maduo rupture (Liu-Zeng et al., 2024), with three main distinct sections that are separated by two major fault bends, respectively located at longitude 97.9°E and 99.0°E. The central section strikes WNW-ESE (~N105), whereas the Eastern and Western sections strike E-W (~N84 and ~N94, respectively). The width of the surface deformation also varies significantly along the 160-km long rupture area. Narrow deformation regions that correlate with the localized ground ruptures are observed along the NW and SE sections of the rupture (red lines in Fig. 1b, and black lines in Fig. 2a). In other regions, meter-scale displacements can be accommodated over a few hundreds of meters to kilometers wide zones (Fig. 2a), correlating with areas where numerous distributed fractures were mapped in the field, and often a lack of primary fault rupture (Fig. 2b; Han et al., 2024; Yuan et al., 2022). We refer to this phenomenon as the so called *diffuse deformation* (Antoine et al., 2021, 2022). In the case of the 2021 Maduo earthquake, diffuse deformation appears dominant along the epicentral area (Figs. 1a and 2b).

4.2. Surface displacement budget, and evolution of the FZW

Total displacements along the 2021 Maduo rupture derived from the analysis of the 781 across-fault profiles (black curve; Fig. 3a,b) evolve between 1 m and 4 m (with the exception of the two rupture tips where displacement tapers to zero), with the smallest displacement values reported in the epicentral area (−20 km to +10 km). In comparison, the largest surface displacements are measured along the eastern and western sections of the rupture. On average, total surface displacement is 2.35 ± 0.09 m, and occurs over a total Fault Zone Width (FZW) ranging between 30 m and 2215 m, corresponding to an average FZW of 600 m.

The localized component of the deformation (red curve and lightered area; Fig. 3a) is primarily detected along the eastern (+30 km to +80 km) and western sections (−30 km to −70 km), where the greatest total surface displacements were also measured. This observation highlights a correlation between the localization of the surface deformation and the increase in total surface displacement for this event. Along the central section of the rupture, few offsets were detected, which is consistent with the field observations (colored points; Fig. 3b). When averaged along the 2021 Maduo rupture length, localized deformation represents 0.62 ± 0.05 m, so 26 % of the total surface displacement, and occurs over an average width of 87 m. The localized deformation curve represents the maximum envelope of the field data as it is usually observed for optical measurements (Antoine et al., 2021; Milliner et al., 2016). Indeed, because of the smoothing effects of the method, offsets retrieved from OIC measurements often include part of the OFD occurring in the vicinity of faults in addition to the slip that occurred on these faults. This smoothing effect can range from a few meters to a few hundreds of meters, and is dependent on the data resolution and on the correlation method and parameterization (Antoine and Liu, 2025; Montagnon et al., 2024). In the present study, this smoothing effect is however limited due to the combination of high-resolution images (0.5 m for the pre-even images, and 1.6 m for the post-event images), cross-correlated at a combined ground resolution of 0.5 m with a correlation window of 2.5 m.

Unlike the localized deformation, OFD is observed along the entire Maduo rupture (grey area; Fig. 3a,b). However, it is dominant along the epicentral region where only limited localized surface slip was detected in the image correlation results (Fig. 3a) as well as in the field (Fig. 3b,c). OFD has the largest amplitude in the epicentral area, up to ~2 m. When averaged along the entire rupture length, OFD represents 1.73 m, so 74 %, of the total surface displacement budget for this event, and it occurs over an average width of 380 m around the localized deformation regions. OFD sometimes occurs in the vicinity of the primary fault ruptures, and affects areas of a few tens to a few hundreds of meters wide that often correlate with regions of distributed fractures or wider shear zones identified in the field (Fig. 2a, and profiles AA' to CC' in Fig. 2c). OFD can also have a wider extent (> 0.5 km), and a non-direct association with ground ruptures, which corresponds to the diffuse deformation regions (e.g., Fig. 2b). Profile DD' in Fig. 2c is a typical example of such a wide deformation region. In this area, no primary surface rupture is visible, but widely scattered en-echelon shear fractures (Han et al., 2024) and shaking-related lateral-spreading features (Yuan et al., 2022) could be mapped. Along the entire Maduo rupture, variations in the relative contributions of localized deformation on faults and OFD along the 2021 Maduo rupture are consistent with that of the total FZW, which shows maximum values up to 2.1 km along the epicentral diffuse deformation region, and minimum values down to 30.0 m along the dominantly localized deformation regions, for example from −40 km to −30 km (Fig. 3d).

Eventually, we also assess the coefficient of variations (CV), corresponding to the standard deviation over the mean, for the different displacement curves. We observe a decrease from a CV of 1.4 for the localized deformation, to a CV of 0.29 for the total displacement curves. The high CV of the localized deformation curve is consistent with the complexity of the surface ruptures and the scattering of the field offsets (e.g., Han et al., 2024; Yuan et al., 2022; Fig. 3b,c). Though, that complexity is not reflected in the total displacement curve that has a lower CV, highlighting the crucial role of OFD in accommodating the total co-seismic surface displacement in regions of lesser surface fault slip (Antoine et al., 2022).

4.3. Across-fault displacement gradient analysis

We derive the displacement gradient ∇d across the localized and OFD regions, respectively, as a first order estimation of the amount of strain accommodated by each deformation region. This allows comparing our surface observations to laboratory measurements and mechanical models (see Section 4.4). ∇d corresponds to the ratio between the amplitude and the width of the offset measured respectively across the localized deformation and OFD regions (see Fig. 2c for examples). The statistical analysis of the ∇d values reveals a median 0.3 % for the OFD with a lower (Q1) and upper (Q3) quartiles of 0.2 % and 0.6 %, respectively (Fig. 3f). In the epicentral region, ∇d of the OFD is uniformly below 0.3 %. ∇d associated with the localized deformation dominantly ranges between 1.2 % (Q1) and 3.3 % (Q3), with a median of 1.9 % (Fig. 3e). These estimates of ∇d for the localized deformation correspond to lower bounds as strain on meter to sub-meter wide slip surfaces cannot be resolved in our data, with a lowest FZW of 30 m resolved in this study. On average, the measured ∇d are consistent with those from C. Li et al. (2023) who detected shear strains of 0.7–5 %, considering that the authors ignored regions of diffuse deformation in their measurements. Using Sentinel-2 OIC results from C. Li et al. (2022), Zhao et al. (2023a) calculated the shear strain across the diffuse deformation regions as low as 0.1–0.2 %, therefore supporting our measurements in these regions. The fact that the shear strain values from Zhao et al. (2023a) are consistent with the displacement gradient values we derived also suggest a limited contribution of rotation to the strike-slip displacement, but rather a dominant role of the shear deformation.

4.4. Conditions for macroscopic yielding

The consideration of low-strain deformation as inelastic has been debated as it occurs below the 0.5 % threshold usually considered for inelastic strain (e.g., Barnhart et al., 2020; Li et al., 2023; Scott et al., 2018). However, building on previous works by Simons and Fialko (2002) and Fialko et al. (2005), more recent studies started considering this low-strain deformation as potentially inelastic strain that could account for slip deficits along shallow rupturing faults (e.g., Antoine et al., 2024; Jin et al., 2023; C. Li et al., 2022; Liu et al., 2025). In the following, we investigate whether the diffuse deformation could have an inelastic contribution, and correspond, at least partially, to macroscopic yielding.

We first use simple mechanical formulations to assess the conditions favorable to yielding in the shallow crust, and whether these conditions are applicable to the case of the 2021 Maduo surface rupture. We consider the displacement gradients measured along the 2021 Maduo rupture (Fig. 3e) to be equivalent to the strain, thus ignoring any rotational component. This is supported by the consistency we previously highlighted between our displacement gradient measurements, and the strain measurements from Li et al. (2023) and Zhao et al. (2023a) for the localized and diffuse deformation, respectively. We take the example of a 0.3 % surface strain, which corresponds to the upper range of ∇d values observed for the diffuse deformation along the epicentral area (Fig. 3e). We then estimate the associated shear stress change ($\Delta\sigma$) in the shallow crust using the following equation:

$$\Delta\sigma = 2 \times \mu \times \Delta\varepsilon \quad (4)$$

with μ the shear modulus, and $\Delta\varepsilon$ the coseismic strain (Jaeger et al., 2007).

In a simple configuration with sandstones in superficial conditions that have a shear modulus of ~5–20 GPa (Fjær, 2009; Lei et al., 2019; Ord et al., 1991), 0.3 % of surface strain corresponds to a shear stress change of 30 to 120 MPa. Such shear stress change is likely sufficient to generate inelastic deformation (Baud et al., 2021; Cilona et al., 2012), though they represent maximum estimates given a purely elastic assumption, and would decrease if adding the inelastic component of the deformation. We combine Eqs. (3) and 4, to assess CF from the measured surface strain of 0.3 %. In superficial conditions, normal stress approaches zero and the yield strength is about the rock cohesion (Jaeger et al., 2007). In the case of a sandstone with a cohesion of ~2 to 5 MPa, we respectively estimate that surface strains down to 0.10 to 0.17 % could be inelastic (CF>1). This strain threshold is consistent with the lower threshold of the diffuse deformation measured along the 2021 Maduo rupture (Fig. 3e).

This analysis is sensitive to variations in mechanical properties of rocks within the upper fault zone, especially due to the presence of unconsolidated sediments and fluids, and the accumulation of damage and healing. We therefore calculate *CF* for a wide range of rock shear moduli and depths to assess the conditions favorable to yielding (Fig. 4). For a given type of rock in given pressure conditions, one can then infer which values of stress change are favorable or unfavorable to yielding. Given the current assumptions on the bulk friction and density, and the measured strain, our results show that yielding is possible for a wide range of rock properties and depths (Fig. 4, blue domain) which are all compatible with a wide range of rock shear moduli in shallow conditions (~5–20 MPa). An increase in the rock shear moduli with depth, as observed in laboratory experiments (Fjær, 2009; Lei et al., 2019) would extend the domain of yielding towards deeper depth for a similar observed surface strain (0.3 % here). Conversely, for lower shear moduli, as often observed within damaged fault zones (e.g., Qiu et al., 2021; Vidale and Li, 2003), the yielding region becomes shallower to accommodate a similar surface strain. Overall, this analysis shows that yielding is a possible mechanism explaining the surface diffuse deformation along the Maduo rupture, possibly accounting for the shallow slip deficit of the 2021 Maduo rupture (Jin et al., 2023).

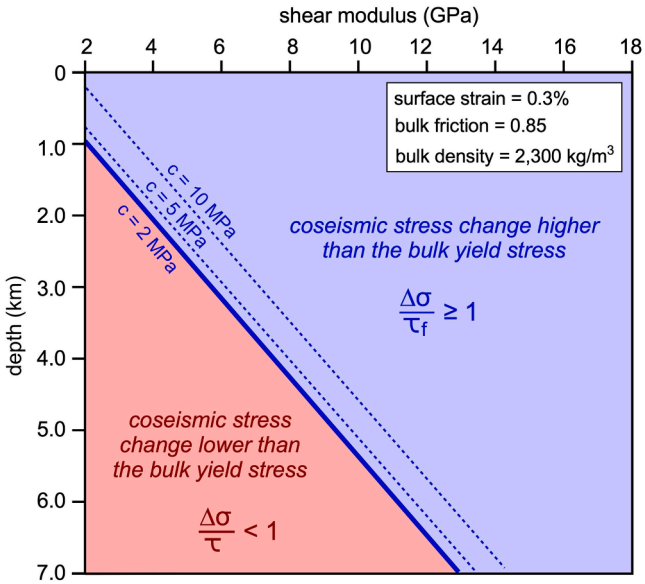

Fig. 4. Evolution of the closeness to failure (CF) with depth and shear modulus for a surface strain of 0.3 %, a bulk density of 2300 kg/m^3, a cohesion of 2 MPa, and a frictional coefficient of 0.85 (for normal stresses below 200 MPa; Byerlee, 1978). Yielding occurs for ***CF*** > 1 line (blue domain). The blue line corresponds to the downdip end of the yielding region for a given bulk shear modulus. The yielding domain increases when reducing the frictional coefficient, and has a low sensitivity to changes in the bulk density. The line CF=1 is also plotted for a bulk cohesion of 5 and 10 MPa.

4.5. Modeling of the shallow crustal deformation

We now attempt to predict the area of yielding based on slip distributions proposed for the 2021 Maduo earthquake, along with additional synthetic slip distributions following the BEM approach from Mallick and Meade (2024) (Fig. 5a). We focus on the epicentral area of the 2021 Maduo rupture, where the surface deformation is entirely diffuse. In this area, Zhao et al. (2023a) proposed a slip of 2 m buried at ~3 km depth, with the top of the slip patch reaching ~0.5 km below the surface. We run tests for this configuration, along with three end-member configurations including i) a deeply buried rupture, ii) a partially buried rupture, and iii) a fully through-going rupture. Zhao et al. (2023a) consider a fully elastic medium in their inversion, although considering elastoplastic deformation would yield a shallower depth for the top of the slip patch (Nevitt et al., 2020), which we also test for (Fig. S7a). For the different scenarios, we predict the closeness to failure from the modeled stress tensor and Eq. (4). The lithology along the Maduo rupture consists in sandstones, mudstones and shales (Han et al., 2024; J. Ren et al., 2022) with a shear modulus in superficial conditions of ~5–20 GPa (Fjær, 2009; Lei et al., 2019; Ord et al., 1991). For the main model, we therefore consider a shear modulus of 10 GPa, a friction of 0.85 (for normal stresses below 200 MPa; Byerlee, 1978), and a cohesion of 2 MPa corresponding to a sandstone in shallow crustal conditions. We assess the isolated effect of each parameter on the predicted yielding area, which overall increases with increasing shear modulus and decreasing friction, and shows low sensitivity to the bulk cohesion (Figure S7).

Results show that yielding within the shallow crust occurs for all scenarios except for the two endmember scenarios of i) a deeply buried rupture, which configuration does not match the 2021 Maduo rupture, and ii) a throughgoing rupture with maximum slip at the surface, which corresponds to the region of dominant localized deformation (e.g., −40 km to −30 km in Fig. 3). Output model for the scenario corresponding to

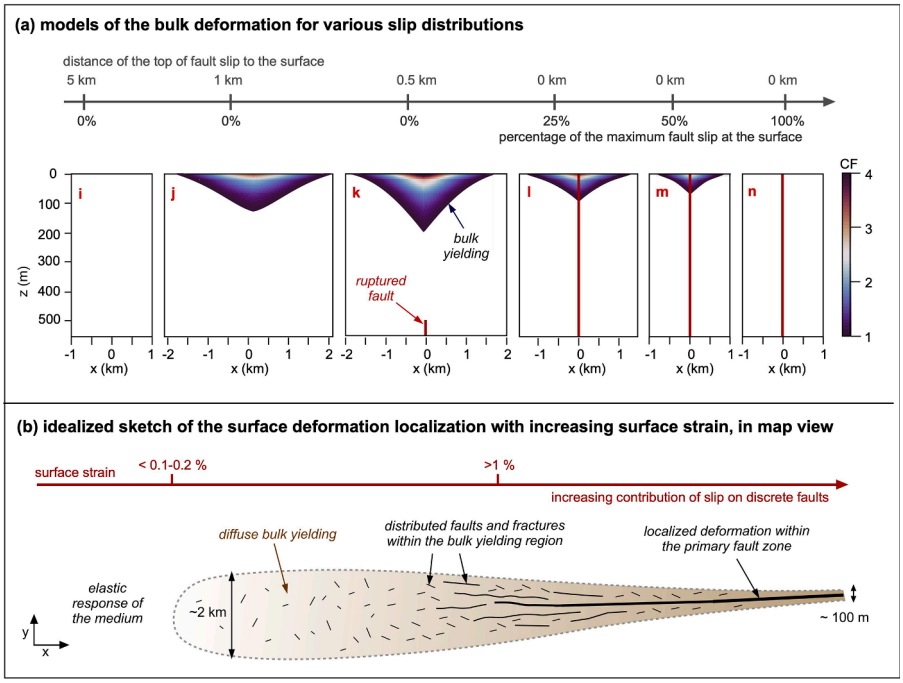

Fig. 5. (a) Predicted yielding area and amplitude using the BEM approach. Yielding occurs where the Closeness to Failure (CF) is above 1 (blue to red colors). Because slip is input in the model as a boundary condition, high CF values do not imply a likelihood of faulting, but signifies that yielding would account for the modeled stress change in the medium. Yielding does not occur when the rupture is too deep (scenario i) or when maximum slip reached the surface (scenario n). In this latter case, yielding due to the dynamic stress change, commonly referred to as damage, would occur but is not represented in this model. (b) Idealized sketch, in map view, of the evolution of the surface deformation with increasing total surface displacement, from a diffuse ($\nabla \boldsymbol{d}$ > 0.1–0.2 %) to a localized ($\nabla \boldsymbol{d}$> 1 %) deformation mode. Strain values indicated on the x-axis do not evolve linearly.

the Maduo epicenter area (Fig. 5a, scenario k) displays a possible yielding region (CF≥1) of 3.5 km-wide, and 0.2 km-deep. This predicted area is wider at the surface than the observed diffuse deformation region of ~1–1.5 km, and shallower than the depth of yielding inferred in Fig. 4. Though, the shape of the predicted yielding area would likely to evolve if considering a depth dependent shear modulus and friction coefficient, not accounted for in this model (Fig. S7). In fact, increasing the shear modulus and decreasing the friction with increasing depth, consistently with the laboratory measurements (Fjær, 2009; Lei et al., 2019; Byerlee, 1978), would deepen the region of yielding towards approaching the depth at which slip tappers on the main fault.

These models only represent the stress change within the off-faut medium and whether it is favorable to yielding given specific bulk mechanical conditions. We do not attempt modeling the absolute stresses within the off-fault medium that, even though it would modulate the amplitude and distribution of yielding, requires information on the pre-stress conditions that are not available for this fault, nor most active faults. We do not consider either the effect of the regional stress tensor, which was rather shown to control the ratio of on- and off-fault deformation (Gabriel et al., 2024). Indeed, along the central section of the 2021 Maduo earthquake, the relative orientation of the fault to the maximum horizontal stress was shown to be less favorable to slip and more prone to distributed and diffuse shear (Liu-Zeng et al., 2024).

In conclusion, despite these simplifications, the width of yielding area predicted in our model is consistent, to a first order, with observations of coseismic surface diffuse deformation (e.g., Antoine et al., 2021; Han et al., 2024; Provost et al., 2024), coseismic fracture distribution (Nurminen et al., 2020; Rodriguez Padilla and Oskin, 2023), and cumulative damage from field observations (Shelef and Oskin, 2010; Wu et al., 2024), seismic imaging (Alongi et al., 2024; Qiu et al., 2021), and aftershock analysis (Perrin et al., 2021; Ross et al., 2019). Eventually, our model predicts bulk yielding driven only by static stress changes. Dynamic stresses during rupture propagation can cause additional OFD, especially in regions of high-slip (Kaneko and Fialko, 2011; Roten et al., 2017; Taufiqurrahman et al., 2023) and geometrical complexity (Klinger et al., 2018; Xi et al., 2025). However, modeling these effects requires costly elastodynamic simulations, uncertain friction laws and constitutive descriptions of bulk plasticity, and it is beyond the scope of this study.

From this analysis, we propose a conceptual model that describes the evolution of the surface deformation localization along the 2021 Maduo rupture as a function of surface strain (Fig. 5b), itself function of the fault slip distribution at depth (Fig. 5a). This simple model illustrates the relation between results from our observations and modeling results, and described an evolution from wide yielding in regions for which maximum slip remained buried at shallow depth, to narrow to no yielding in regions where maximum slip reached the surface. This model does not exclude the presence of near-fault damage triggered by dynamic stresses, which is likely included within both the localized deformation and OFD measurements. Extrapolated at the scale of several seismic cycles, the accumulation of yielding would participate to the long-term building of the fault zone structure which localizes incrementally with cumulative coseismic displacement (Perrin et al., 2016) until it reaches a steady width related to persistent fault complexity (Visage et al., 2023).

5. Discussion

5.1. Contribution of yielding to the diffuse OFD

Our surface observations along the 2021 Maduo rupture reveal that 74 % of the surface displacement budget is accommodated by OFD occurring both along the surface-rupturing sections, to the exceptions of a few sections where all the displacement localizes along the mapped ground ruptures, and along the regions of primary rupture gaps where OFD is represented by km-wide diffuse deformation (Figs. 3a,b). Across the regions of wide diffuse deformation, although no continuous throughgoing rupture could be found, distributed shear cracks were

mapped (Han et al., 2024; Yuan et al., 2022). Shear strain across these regions range between 0.1 and 0.3 % (Fig. 3e; Zhao et al., 2023a), which is below the ~0.5 % value usually considered as the minimum threshold for surface inelastic strain (e.g., Barnhart et al., 2020; Li et al., 2023; Scott et al., 2018). This threshold is derived from measurement of the axial strain associated with the macroscopic failure of rocks samples in laboratory experiments (e.g., Morrow and Lockner, 2006). Because of the possibility to fit the km-scale diffuse deformation signal using a pure-elastic assumption (e.g., Nevitt et al., 2020; Zhao et al., 2023a), it has generally been considered as purely elastic. However, considering the diffuse deformation as elastic implies a stress build up in the shallow crust due to the deficit in shallow slip and therefore, of shallow inelastic strain (SSD; Fialko et al., 2005). In this configuration, this SSD then has to be accounted for by afterslip, creep, or future shallow fault ruptures.

However, along the central section of the Maduo rupture where diffuse deformation is dominant, surface afterslip is limited to 0.35 m within the first year after the event (Jin et al., 2023; L. Zhao et al., 2023). This afterslip is included in our measurements of diffuse deformation in this area since our post-event data were acquired about a year after the earthquake (Tab. S1). On average, afterslip measured ~1 year after the earthquake represents less than ~20 % of the average diffuse deformation measured for that event (Fig. 3a). Because afterslip evolves logarithmically with time (Marone et al., 1991; Scholz, 1998), its contribution will become even more negligeable with time, making it unlikely to ever account for the SSD. Moreover, InSAR observations do not have the spatial resolution to determine whether this shallow near-fault post-seismic deformation corresponds to localized afterslip on a descrete fault or to bulk deformation. Actually, our higher resolution optical observations (Fig. 2b) as well as field studies conducted in the months (Han et al., 2024; J. Ren et al., 2021; J. 2022; Yuan et al., 2022) after the earthquake did not detect localized features in these regions, suggesting that the shallow post-seismic deformation in the epicentral area occurs through poro-elastoplastic deformation of the bulk (Abdelmeguid et al., 2024; Lindsey et al., 2014; Mia et al., 2023).

Additionally, no interseismic surface creep was detected along the Jiangcuo fault (Fang et al., 2022), suggesting that the shallow parts of the fault are locked during the inter-seismic period. Even though, we cannot entirely rule out the possibilities that creep could occur at very low rate (under the InSAR detection limit of ~2–3 mm/yr; Higgins and Wdowinski, 2025) or at other times of the inter-seismic period through more transient events, the fact that the 2021 event did not trigger detectable creep on the Jiangcuo fault suggest that this fault is not favorable to creep from start. One could finally argue that the stress accumulated in the shallow crust over time would be released during a later earthquake. Such complementarity between shallow and deeper events on non-creeping continental faults has been observed (Thompson Jobe et al., 2025), but the limited number of examples suggests it is an isolated phenomenon.

The low likelihood of all the previously listed processes calls for another process to explain the diffuse deformation signal, with macroscopic yielding being a primary candidate as suggested by our mechanical analysis and modeling (Fig. 4 and 5). Though, our analysis does not exclude a dual source for the diffuse deformation, with both elastic and inelastic deformations contributing to the observed surface displacements. The exact contributions of elastic and inelastic strain to the observed diffuse deformation still remains to be constrained using more advanced modeling calibrated over geological data, and would have critical implications for our understanding of the earthquake and fault zone deformation budget.

5.2. Intricate relations between OFD and SSD

From a theoretical perspective, surface diffuse deformation is directly correlated to the presence of a SSD whether we consider it elastic or elastoplastic (Fialko et al., 2005; Nevitt et al., 2020; Fig. 5a). However, this relation is more intricate in natural observations because of numerous factors. First, definitions and measurement scales of OFD vary among studies, especially because of the large diversity of data type (field versus geodesy) and resolutions. In fact, most studies document the high-amplitude off-fault displacement gradients occurring in the first tens to hundreds of meters around the main ruptures (e.g., Barnhart et al., 2020; Li et al., 2023; Milliner et al., 2021, 2025, 2016; Teran et al., 2015), and usually ignore the contribution of the larger-scale diffuse deformation that requires producing displacement maps covering both the near- and far-field to measure offsets over a larger across-fault aperture (Antoine et al., 2021, 2022; Li et al., 2022; Liu et al., 2025; Provost et al., 2024; Xi et al., 2025). However, the near-fault OFD is likely to be dominantly controlled by dynamic stress effects, and to increase with fault slip (e.g., Faulkner et al., 2011; Savage and Brodsky, 2011) whereas the larger-scale diffuse OFD is rather controlled by the static stress change due to the partially or totally buried rupture (Fig. 5). Then, the correlation with SSD occurs only for the diffuse component of the OFD, provided that the models are well constructed and constrained (Antoine et al., 2024; Liu et al., 2025), whereas the near-fault dynamically triggered OFD would most likely not correlate (Milliner et al., 2025). Varying model resolutions and accuracies, especially in the shallow crust, usually prevent detailed comparison between measurements and models. Because of the smoothing effect of correlation methods, part of the near-fault OFD is also included in the measured offsets, and then represented as slip in the inversions.

Along the Maduo rupture, a ~30 % average SSD was assessed from inversion of SAR measurement (Jin and Fialko, 2021; Li et al., 2025; Tong et al., 2022). SSD in the model from Tong et al. (2022) is larger along the central stretch of the rupture, which is supported by Zhao et al. (2023a) who used optical data to constrain the shallow (0–3 km) slip distribution. Here, the average SSD is less than half the proportion of OFD measured at the surface (74 %). This difference primarily lies in the fact that OFD measurement from this study, like those from Li et al. (2022), include both the near-fault and diffuse components of OFD together. In addition, the models that estimate SSD are based only on SAR data, and therefore might include part of the OFD in the modeled slip. For these reasons, we cannot directly relate the amount of modeled SSD to that of measured OFD. Still, the fact that Tong et al. (2022) and Zhao et al. (2023a) propose a larger SSD along the central section of the rupture is consistent with the larger or even dominant contribution of diffuse OFD we measured in that area.

Conclusions

We present high-resolution measurements of the surface displacements along the 2021 M_w7.4 Maduo, Tibet, rupture, obtained from the sub-pixel cross-correlation of Pleiades and SPOT6/7 satellite images. These measurements allow for detailed quantification of the surface displacement along the Maduo fault zone, including the total surface deformation, and the respective contributions of the localized and off-fault deformations. Results show:

- Localized deformation is a minor component of the surface deformation along the 2021 Maduo rupture, whereas OFD contributed, on average, to ~74 %.
- Kilometer-wide diffuse deformation is dominant within the first 30 km around the earthquake epicenter, whereas other regions of the rupture present partly localized deformation on primary or secondary fault ruptures.
- Displacement gradients associated with the diffuse deformation range between 0.1 and 0.3 %, which is below the commonly used inelastic strain threshold inferred from laboratory observations of macroscopic rock failure.
- Using simple mechanical formulations, supported by a 2D modeling approach, we show that low-strain diffuse deformation can correspond to elastoplastic yielding. Our models reproduce the spatial

scale of the surface diffuse deformation, and are valid through a wide range of rock mechanical properties.
- The lack of surface afterslip and/or creep along the diffuse deformation regions support our interpretations that the diffuse deformation may include an inelastic component, and account for part of the shallow slip deficit.

In conclusion, this study shows that the diffuse deformation partly reflects macroscopic crustal yielding accounting for the lack of shallow slip in some regions of the 2021 Maduo rupture, especially along the epicentral region. This example shows that diffuse deformation should be accounted for in the surface deformation budget of continental earthquake ruptures, at least those that partially ruptured the ground surface.

Open research

The Pleiades images were provided by the DINAMIS program from CNES (https://dinamis.teledetection.fr; https://cnes.fr; last accessed on 01/03/24). The SPOT6/7 images were provided by the DINAMIS program and ForM@Ter pole (https://en.poleterresolide.fr; last accessed on 01/03/2024) from CNES. Sentinel2 images were accessed at https://dataspace.copernicus.eu/ (last accessed on 01/03/24). Detailed information on the image references, dates, and catalogues are provided in Supplementary Table S1 and S2. MicMac (https://github.com/micmacIGN/micmac; last accessed on 01/03/24) and StackProf (https://github.com/IPGP/stackprof; last accessed on 01/03/24) are open source. Codes for the Boundary Element Modeling approach are available at https://github.com/mallickrishg/bemcs/tree/main (last accessed on 04/19/25). Supplementary figures providing details on the methodology and on the results of this study are available in the electronic supplements. Surface displacement maps, and fault displacement measurements are available on Figshare at the following link: https://doi.org/10.6084/m9.figshare.31116355.

Declaration of competing interest

The authors declare the following financial interests/personal relationships which may be considered as potential competing interests: Zhen Liu reports financial support was provided by National Aeronautics and Space Administration. Yann Klinger reports financial support was provided by French National Research Agency. If there are other authors, they declare that they have no known competing financial interests or personal relationships that could have appeared to influence the work reported in this paper.

Acknowledgments

This work was carried out at the Jet Propulsion Laboratory, California Institute of Technology, under a contract with the National Aeronautics and Space Administration (80NM0018D0004). This work was supported by NASA Decadal Survey Incubator/Surface Topography and Vegetation program, and the ANR-18-CE31-0012 project. Satellite imagery was mainly acquired through the TOSCA and CIEST2 CNES programs. This study contributed to the IdEx Université de Paris ANR-18-IDEX-0001. Numerical computations were performed on the GATTACA (JPL, USA), and S-CAPAD/DANTE (IPGP, France) platforms. © 2026. California Institute of Technology. Government sponsorship acknowledged.

Supplementary materials

Supplementary material associated with this article can be found, in the online version, at doi:10.1016/j.epsl.2026.119868.

References

Abdelmeguid, M., Elbanna, A., 2022. Modeling sequences of earthquakes and aseismic slip (SEAS) in Elasto-plastic fault zones with a hybrid finite element spectral boundary integral scheme. J. Geophys. Res.: Solid Earth 127, e2022JB024548. https://doi.org/10.1029/2022JB024548.

Abdelmeguid, M., Mia, M.S., Elbanna, A., 2024. On the interplay between distributed bulk plasticity and local fault slip in evolving fault zone complexity. Geophys. Res. Lett. 51, e2023GL108060. https://doi.org/10.1029/2023GL108060.

Alongi, T., Brodsky, E.E., Kluesner, J., Brothers, D., 2024. Characteristics of the fault damage zone from high-resolution seismic imaging along the Palos Verdes fault, California. AGU Adv. 5, e2023AV001155. https://doi.org/10.1029/2023AV001155.

Antoine, S.L., Liu, Z., 2025. Impact of optical imagery and topography data resolution on the measurement of surface fault displacement using sub-pixel image correlation. Earth Space Sci. In press.

Antoine, S.L., Klinger, Y., Wang, K., Bürgmann, R., 2024. Coseismic shallow slip deficit accounted for by diffuse off-fault deformation. Geophys. Res. Lett. https://doi.org/10.1029/2024GL110798.

Antoine, S.L., Klinger, Y., Delorme, A., Gold, R.D., 2022. Off-fault deformation in regions of complex fault geometries: the 2013, Mw7.7, Baluchistan rupture (Pakistan). J. Geophys. Res. Solid Earth 127, e2022JB024480. https://doi.org/10.1029/2022JB024480.

Antoine, S.L., Klinger, Y., Delorme, A., Wang, K., Bürgmann, R., Gold, R.D., 2021. Diffuse deformation and surface faulting distribution from submetric image correlation along the 2019 Ridgecrest, California. Ruptures. Bull. Seism. Soc. Am 111, 2275–2302. https://doi.org/10.1785/0120210036.

Barnhart, W.D., Gold, R.D., Hollingsworth, J., 2020. Localized fault-zone dilatancy and surface inelasticity of the 2019 Ridgecrest earthquakes. Nat. Geosci. 13, 699–704. https://doi.org/10.1038/s41561-020-0628-8.

Baud, P., Hall, S., Heap, M.J., Ji, Y., Wong, T.-f., 2021. The brittle-ductile transition in porous limestone: failure mode, constitutive modeling of inelastic deformation and strain localization. J. Geophys. Res.: Solid Earth 126, e2020JB021602. https://doi.org/10.1029/2020JB021602.

Byerlee, J., 1978. Friction of rocks. Pure Appl. Geophys 116, 12. PAGEOPH.

Chen, K.H., Bürgmann, R., 2017. Creeping faults: good news, bad news? Rev. Geophys. 55, 282–286. https://doi.org/10.1002/2017RG000565.

Cilona, A., Baud, P., Tondi, E., Agosta, F., Vinciguerra, S., Rustichelli, A., Spiers, C.J., 2012. Deformation bands in porous carbonate grainstones: field and laboratory observations. J. Struct. Geol. 45, 137–157. https://doi.org/10.1016/j.jsg.2012.04.012.

Delorme, A., Grandin, R., Klinger, Y., Pierrot-Deseilligny, M., Feuillet, N., Jacques, E., Rupnik, E., Morishita, Y., 2020. Complex deformation at shallow depth during the 30 October 2016 Mw6.5 Norcia earthquake: interference between tectonic and gravity processes? Tectonics 39, 005596. https://doi.org/10.1029/2019TC005596, 2019.

Fan, X., Zhang, G., Zhao, D., Xie, C., Huang, C., Shan, X., 2022. Fault geometry and kinematics of the 2021 Mw 7.3 Maduo earthquake from aftershocks and InSAR observations. Front. Earth Sci. 10, 993984. https://doi.org/10.3389/feart.2022.993984.

Fang, J., Ou, Q., Wright, T.J., Okuwaki, R., Amey, R.M.J., Craig, T.J., Elliott, J.R., Hooper, A., Lazecký, M., Maghsoudi, Y., 2022. Earthquake cycle deformation associated with the 2021 MW 7.4 Maduo (Eastern Tibet) Earthquake: an intrablock rupture event on a slow-slipping fault from sentinel-1 InSAR and teleseismic data. J. Geophys. Res. Solid Earth 127, e2022JB024268. https://doi.org/10.1029/2022JB024268.

Faulkner, D.R., Mitchell, T.M., Jensen, E., Cembrano, J., 2011. Scaling of fault damage zones with displacement and the implications for fault growth processes. J. Geophys. Res. Solid Earth 116, 05403. https://doi.org/10.1029/2010JB007788.

Fialko, Y., Sandwell, D., Simons, M., Rosen, P., 2005. Three-dimensional deformation caused by the Bam, Iran, earthquake and the origin of shallow slip deficit. Nature 435, 295–299. https://doi.org/10.1038/nature03425.

Fjær, E., 2009. Static and dynamic moduli of a weak sandstone. Geophysics 74. https://doi.org/10.1190/1.3052113. WA103–WA112.

Gold, R.D., Reitman, N.G., Briggs, R.W., Barnhart, W.D., Hayes, G.P., Wilson, E., 2015. On and off-fault deformation associated with the September 2013 Mw 7.7 Balochistan earthquake: implications for geologic slip rate measurements. Tectonophysics 660, 65–78. https://doi.org/10.1016/j.tecto.2015.08.019.

Han, L., Liu-Zeng, J., Yao, W., Wang, W., Shao, Y., Liu, X., Zeng, X., Gao, Y., Tu, H., 2024. Discontinuous surface ruptures and slip distributions in the epicentral region of the 2021 Mw7.4 Maduo Earthquake, China. Remote Sens. 16, 1250. https://doi.org/10.3390/rs16071250.

Harris, R.A., 2017. Large earthquakes and creeping faults. Rev. Geophys. 55, 169–198. https://doi.org/10.1002/2016RG000539.

He, K., Wen, Y., Xu, C., Zhao, Y., 2021. Fault geometry and slip distribution of the 2021 Mw 7.4 Maduo, China, earthquake inferred from InSAR measurements and relocated aftershocks. Seism. Res. Lett. 93, 8–20. https://doi.org/10.1785/0220210204.

Higgins, M., Wdowinski, S., 2025. InSAR detection of slow ground deformation: taking advantage of sentinel-1 time series length in reducing error sources. Remote Sens. 17, 2420. https://doi.org/10.3390/rs17142420.

Idini, B., Ampuero, J.-P., 2020. Fault-zone damage promotes pulse-like rupture and back-propagating fronts via quasi-static effects. Geophys. Res. Lett. 47, e2020GL090736. https://doi.org/10.1029/2020GL090736.

Jaeger, J.C., Cook, N.G.W., Zimmerman, R., 2007. Fundamentals of rock mechanics. Wiley.

Jin, Z., Fialko, Y., 2021. Coseismic and early postseismic deformation due to the 2021 M7.4 Maduo (China) earthquake. Geophys. Res. Lett. 48. https://doi.org/10.1029/2021GL095213.

Jin, Z., Fialko, Y., Yang, H., Li, Y., 2023. Transient deformation excited by the 2021 M7.4 Maduo (China) earthquake: evidence of a deep shear zone. J. Geophys. Res. Solid Earth 128, e2023JB026643. https://doi.org/10.1029/2023JB026643.

Jolivet, R., Lasserre, C., Doin, M.-P., Guillaso, S., Peltzer, G., Dailu, R., Sun, J., Shen, Z.-K., Xu, X., 2012. Shallow creep on the Haiyuan Fault (Gansu, China) revealed by SAR Interferometry. J. Geophys. Res.: Solid Earth 117. https://doi.org/10.1029/2011JB008732.

Kanamori, H., Brodsky, E.E., 2004. The physics of earthquakes. Rep. Prog. Phys. 67, 1429–1496.

Kaneko, Y., Fialko, Y., 2011. Shallow slip deficit due to large strike-slip earthquakes in dynamic rupture simulations with elasto-plastic off-fault response: modelling shallow slip deficit. Geophys. J. Int. 186, 1389–1403. https://doi.org/10.1111/j.1365-246X.2011.05117.x.

King, G.C.P., Stein, R.S., Lin, J., 1994. Static stress changes and the triggering of earthquakes. Bull. Seismol. Soc. Am. 84, 935–953.

Klinger, Y., Okubo, K., Vallage, A., Champenois, J., Delorme, A., Rougier, E., Lei, Z., Knight, E.E., Munjiza, A., Satriano, C., Baize, S., Langridge, R., Bhat, H.S., 2018. Earthquake damage patterns resolve complex rupture processes. Geophys. Res. Lett. 45, 10279–10287. https://doi.org/10.1029/2018GL078842.

Lei, R., Wang, Yao, Zhang, L., Liu, B., Long, K., Luo, P., Wang, YaKun, 2019. The evolution of sandstone microstructure and mechanical properties with thermal damage. Energy Sci. Eng. 7, 3058–3075. https://doi.org/10.1002/ese3.480.

Leprince, S., Barbot, S., Ayoub, F., Avouac, J.-P., 2007. Automatic and precise orthorectification, coregistration, and subpixel correlation of satellite images, application to ground deformation measurements. Geosci. Remote Sens. IEEE Trans. On. 45, 1529–1558. https://doi.org/10.1109/TGRS.2006.888937.

Li, C., Li, T., Hollingsworth, J., Zhang, Y., Qian, L., Shan, X., 2023. Strain threshold for the formation of coseismic surface rupture. Geophys. Res. Lett. 50, e2023GL103666. https://doi.org/10.1029/2023GL103666.

Li, C., Li, T., Shan, X., Zhang, G., 2022. Extremely large off-fault deformation during the 2021 Mw 7.4 maduo, Tibetan plateau. Earthq. Seism. Res. Lett. https://doi.org/10.1785/0220220139.

Li, Y., Nocquet, J.-M., Shan, X., Song, X., 2021. Geodetic observations of shallow creep on the Laohushan-Haiyuan Fault, northeastern Tibet. J. Geophys. Res.: Solid Earth 126, e2020JB021576. https://doi.org/10.1029/2020JB021576.

Li, Z., Li, C., Wang, T., 2025. Along-dipping variations in fault geometry influencing shallow-slip-deficit during the 2021 *M*W7.4 Maduo earthquake. Geod. Geodyn. https://doi.org/10.1016/j.geog.2025.05.001.

Lindsey, E.O., Sahakian, V.J., Fialko, Y., et al., 2014. Interseismic strain localization in the San Jacinto Fault Zone. Pure Appl. Geophys. 171, 2937–2954. https://doi.org/10.1007/s00024-013-0753-z.

Liu, J., Jónsson, S., Li, X., Yao, W., Klinger, Y., 2025. Extensive off-fault damage around the 2023 Kahramanmaraş earthquake surface ruptures. Nat. Commun. 16, 1286. https://doi.org/10.1038/s41467-025-56466-w.

Liu, J., Hu, J., Li, Z., Ma, Z., Wu, L., Jiang, W., Feng, G., Zhu, J., 2022. Complete three-dimensional coseismic displacements due to the 2021 Maduo earthquake in Qinghai Province, China from Sentinel-1 and ALOS-2 SAR images. Sci. China Earth Sci. 65, 687–697. https://doi.org/10.1007/s11430-021-9868-9.

Liu-Zeng, J., Liu, Z., Liu, X., Milliner, C., Padilla, A., Xu, S., Avouac, J.-P., Yao, W., Klinger, Y., Han, L., Shao, Y., Yan, X., Aati, S., Shao, Z., 2024. Fault orientation trumps Fault maturity in controlling coseismic rupture characteristics of the 2021 Maduo earthquake. AGU Adv. 5. https://doi.org/10.1029/2023AV001134.

Mallick, R., Meade, B.J., 2025. Smooth slip is all you need: a singularity-free boundary element method for fault slip problems. Comput. Geosci. 196, 105820. https://doi.org/10.1016/j.cageo.2024.105820.

Marone, C., Scholz, C., Bilham, R., 1991. On the mechanics of earthquake afterslip. J. Geophys. Res. 96, 8441–8452.

McBeck, J., Ben-Zion, Y., Renard, F., 2021. Fracture network localization preceding catastrophic failure in triaxial compression experiments on rocks. Front. Earth Sci. 9.

Mia, M.S., Abdelmeguid, M., Elbanna, A.E., 2023. The spectrum of fault slip in elastoplastic fault zones. Earth Planet. Sci. Lett. 619, 118310. https://doi.org/10.1016/j.epsl.2023.118310.

Milliner, C.W.D., Avouac, J.-P., Aati, S., 2025. Relations between OFD and fault and earthquake characteristics. Nat. Geosci.

Milliner, C.W.D., Dolan, J.F., Hollingsworth, J., Leprince, S., Ayoub, F., 2016. Comparison of coseismic near-field and off-fault surface deformation patterns of the 1992 Mw 7.3 Landers and 1999 Mw 7.1 Hector Mine earthquakes: implications for controls on the distribution of surface strain. Geophys. Res. Lett. 43 (10), 124, 115-10.

Moon, S., Perron, J.T., Martel, S.J., Goodfellow, B.W., Mas Ivars, D., Hall, A., Heyman, J., Munier, R., Näslund, J.-O., Simeonov, A., Stroeven, A.P., 2020. Present-day stress field influences bedrock fracture openness deep into the subsurface. Geophys. Res. Lett. 47, e2020GL090581. https://doi.org/10.1029/2020GL090581.

Montagnon, T., Giffard-Roisin, S., Dalla Mura, M., Marchandon, M., Pathier, E., Hollingsworth, J., 2024. Sub-pixel displacement estimation with deep learning: application to optical satellite images containing sharp displacements. J. Geophys. Res.: Mach. Learn. Comput. 1, e2024JH000174. https://doi.org/10.1029/2024JH000174.

Morrow, C.A., Lockner, D.A., 2006. Physical properties of two core samples from Well 34-9RD2 at the Coso geothermal field, California (No. 2006–1230), open-file report. U.S. Geol. Surv. https://doi.org/10.3133/ofr20061230.

Nevitt, J.M., Brooks, B.A., Catchings, R.D., Goldman, M.R., Ericksen, T.L., Glennie, C.L., 2020. Mechanics of near-field deformation during co and post-seismic shallow fault slip. Sci Rep 10, 5031. https://doi.org/10.1038/s41598-020-61400-9.

Nicolas, A., Fortin, J., Guéguen, Y., 2017. Micromechanical constitutive model for low-temperature constant strain rate deformation of limestones in the brittle and semi-brittle regime. Geophys. J. Int. 211, 300–321. https://doi.org/10.1093/gji/ggx299.

Nurminen, F., Boncio, P., Visini, F., Pace, B., Valentini, A., Baize, S., Scotti, O., 2020. Probability of occurrence and displacement regression of distributed surface rupturing for reverse earthquakes. Front. Earth Sci. 8.

Okubo, K., Bhat, H.S., Rougier, E., Marty, S., Schubnel, A., Lei, Z., Knight, E.E., Klinger, Y., 2019. Dynamics, radiation, and overall energy budget of earthquake rupture with coseismic off-fault damage. J Geophys Res Solid Earth 11771–11801.

Ord, A., Vardoulakis, I., Kajewski, R., 1991. Shear band formation in Gosford Sandstone. Int. J. Rock Mech. Min. Sci. Geomech. Abstr. 28, 397–409. https://doi.org/10.1016/0148-9062(91)90078-Z.

Pan, J., Li, H., Chevalier, M.-L., Tapponnier, P., Bai, M., Li, Chao, Liu, F., Liu, D., Wu, K., Wang, P., Li, Chunrui, Lu, H., Chen, P., 2022. Co-seismic rupture of the 2021, Mw7.4 Maduo earthquake (northern Tibet): short-cutting of the Kunlun fault big bend. Earth Planet. Sci. Lett. 594, 117703. https://doi.org/10.1016/j.epsl.2022.117703.

Perrin, C., Manighetti, I., Ampuero, J.-P., Cappa, F., Gaudemer, Y., 2016. Location of largest earthquake slip and fast rupture controlled by along-strike change in fault structural maturity due to fault growth. J. Geophys. Res. Solid Earth 121, 3666–3685. https://doi.org/10.1002/2015JB012671.

Perrin, C., Waldhauser, F., Scholz, C.H., 2021. The shear deformation zone and the smoothing of faults with displacement. J. Geophys. Res.: Solid Earth 126, e2020JB020447. https://doi.org/10.1029/2020JB020447.

Petit, L., Olive, J.-A., Schubnel, A., Le Pourhiet, L., Bhat, H.S., 2024. A brittle constitutive law for long-term tectonic modeling based on sub-critical crack growth. Geochem., Geophys., Geosyst. 25, e2023GC011229. https://doi.org/10.1029/2023GC011229.

Pousse-Beltran, L., Nissen, E., Bergman, E.A., Cambaz, M.D., Gaudreau, É., Karasözen, E., Tan, F., 2020. The 2020 Mw 6.8 Elazığ (Turkey) earthquake reveals rupture behavior of the east Anatolian fault. Geophys. Res. Lett. 47, e2020GL088136. https://doi.org/10.1029/2020GL088136.

Provost, F., Karabacak, V., Malet, J.-P., Van der Woerd, J., Meghraoui, M., Masson, F., Ferry, M., Michéa, D., Pointal, E., 2024. High-resolution co-seismic fault offsets of the 2023 Türkiye earthquake ruptures using satellite imagery. Sci. Rep. 14, 6834. https://doi.org/10.1038/s41598-024-55009-5.

Qiu, H., Ben-Zion, Y., Catchings, R., Goldman, M.R., Allam, A.A., Steidl, J., 2021. Seismic imaging of the Mw 7.1 Ridgecrest earthquake rupture zone from data recorded by dense linear arrays. J. Geophys. Res.: Solid Earth 126, e2021JB022043. https://doi.org/10.1029/2021JB022043.

Reid, H.F., 1911. The elastic-rebound theory of earthquakes. Univ. Calif. Publ.. Bull. Dept. Geol 6, 413–444.

Reitman, N.G., Mueller, K.J., Tucker, G.E., 2022. Surface slip variability on strike-slip faults. Earth Surf. Processes Landf. 47, 908–935. https://doi.org/10.1002/esp.5294.

Ren, J., Xu, X., Zhang, G., Wang, Q., Zhang, Z., Gai, H., Kang, W., 2022. Coseismic surface ruptures, slip distribution, and 3D seismogenic fault for the 2021 Mw 7.3 Maduo earthquake, central Tibetan Plateau, and its tectonic implications. Tectonophysics 827, 229275. https://doi.org/10.1016/j.tecto.2022.229275.

Ren, J., Zhang, Z., Gai, H., Kang, W., 2021. Typical Riedel shear structures of the coseismic surface rupture zone produced by the 2021 Mw 7.3 Maduo earthquake, Qinghai, China, and the implications for seismic hazards in the block interior. Nat. Hazards Res. 1, 145–152. https://doi.org/10.1016/j.nhres.2021.10.001.

Rodriguez Padilla, A.M., Oskin, M.E., 2023. Displacement hazard from distributed ruptures in strike-slip earthquakes. Bull. Seismol. Soc. Am. https://doi.org/10.1785/0120230044.

Roten, D., Olsen, K.B., Day, S.M., 2017. Off-fault deformations and shallow slip deficit from dynamic rupture simulations with fault zone plasticity. Geophys. Res. Lett. 44, 7733–7742. https://doi.org/10.1002/2017GL074323.

Ross, Z.E., Idini, B., Jia, Z., Stephenson, O.L., Zhong, M., Wang, X., Zhan, Z., Simons, M., Fielding, E.J., Yun, S.-H., Hauksson, E., Moore, A.W., Liu, Z., Jung, J., 2019. Hierarchical interlocked orthogonal faulting in the 2019 Ridgecrest earthquake sequence. Science 366, 346–351. https://doi.org/10.1126/science.aaz0109.

Rosu, A.-M., Pierrot-Deseilligny, M., Delorme, A., Binet, R., Klinger, Y., 2015. Measurement of ground displacement from optical satellite image correlation using the free open-source software MicMac. ISPRS J. Photogramm. Remote Sens. High-Resolut. Earth Imaging Geospatial. Inf. 100, 48–59. https://doi.org/10.1016/j.isprsjprs.2014.03.002.

Rupnik, E., Pierrot-Deseilligny, M., Delorme, A., 2018. 3D reconstruction from multi-view VHR-satellite images in MicMac. ISPRS J. Photogramm. Remote Sens. 139, 201–211. https://doi.org/10.1016/j.isprsjprs.2018.03.016.

Savage, H.M., Brodsky, E.E., 2011. Collateral damage: evolution with displacement of fracture distribution and secondary fault strands in fault damage zones. J. Geophys. Res.: Solid Earth 116. https://doi.org/10.1029/2010JB007665.

Scholz, C.H., 1998. Earthquakes and friction laws. Nature 391, 37–42. https://doi.org/10.1038/34097.

Scott, C.P., Arrowsmith, J.R., Nissen, E., Lajoie, L., Maruyama, T., Chiba, T., 2018. The M7 2016 Kumamoto, Japan, earthquake: 3-D deformation along the fault and within the damage zone constrained from differential lidar topography. J. Geophys. Res. Solid Earth 123, 6138–6155. https://doi.org/10.1029/2018JB015581.

Sethanant, I., Nissen, E., Pousse-Beltran, L., Bergman, E., Pierce, I., 2023. The 2020 Mw 6.5 Monte Cristo Range, Nevada, earthquake: anatomy of a crossing-fault rupture through a region of highly distributed deformation. Bull. Seismol. Soc. Am. 113, 948–975. https://doi.org/10.1785/0120220166.

Shelef, E., Oskin, M., 2010. Deformation processes adjacent to active faults: examples from eastern California. J. Geophys. Res.: Solid Earth 115. https://doi.org/10.1029/2009JB006289.

Simons, M., Fialko, Y., 2002. Coseismic deformation from the 1999 Mw 7.1 Hector Mine, California, earthquake as inferred from InSAR and GPS observations. Bull. Seismol. Soc. America 92 (4), 1390–1402. https://doi.org/10.1785/0120000933.

Taufiqurrahman, T., Gabriel, A.-A., Li, D., Ulrich, T., Li, B., Carena, S., Verdecchia, A., Gallovič, F., 2023. Dynamics, interactions and delays of the 2019 Ridgecrest rupture sequence. Nature 618, 1–8. https://doi.org/10.1038/s41586-023-05985-x.

Thompson Jobe, J.A., Hanagan, C.E., Hatem, A.E., Barnhart, W.D., Goldberg, D.E., Yeck, W.L., 2025. Surface rupture from an aftershock: remote observations from the January 2024 Wushi (Aykol), China, earthquakes. Seismol. Res. Lett. https://doi.org/10.1785/0220240347.

Tong, X., Xu, X., Chen, S., 2022. Coseismic slip model of the 2021 Maduo Earthquake, China from Sentinel-1 InSAR observation. Remote Sensing 14, 436. https://doi.org/10.3390/rs14030436.

Thakur, P., Huang, Y., 2021. Influence of fault zone maturity on fully dynamic earthquake cycles. Geophys. Res. Lett. 48, e2021GL094679. https://doi.org/10.1029/2021GL094679.

Vidale, J.E., Li, Y.-G., 2003. Damage to the shallow Landers fault from the nearby Hector Mine earthquake. Nature 421, 524–526. https://doi.org/10.1038/nature01354.

Visage, S., Souloumiac, P., Cubas, N., Maillot, B., Antoine, S.L., Delorme, A., Klinger, Y., 2023. Evolution of the off-fault deformation of strike-slip faults in a sand-box experiment. Tectonophysics 847, 229704. https://doi.org/10.1016/j.tecto.2023.229704.

Wang, W., Fang, L., Wu, J., Tu, H., Chen, L., Lai, G., Zhang, L., 2021. Aftershock sequence relocation of the 2021 MS7.4 Maduo Earthquake, Qinghai, China. Sci. China Earth Sci. 64, 1371–1380. https://doi.org/10.1007/s11430-021-9803-3.

Wei, S., Zeng, H., Shi, Q., Liu, J., Luo, H., Hu, W., Li, Y., Wang, W., Ma, Z., Liu-Zeng, J., Wang, T., 2022. Simultaneous rupture propagation through fault bifurcation of the 2021 Mw7.4 Maduo earthquake. Geophys. Res. Lett. 49, e2022GL100283. https://doi.org/10.1029/2022GL100283.

Wu, C.H., Cui, P., Klinger, Y., Tan, X.B., Yi, S.J., Li, Y.S., 2024. Pre-existing off-fault damage can restrain coseismic on-fault slip. Geop. Res. Lett. https://doi.org/10.1029/2024GL111198.

Xi, X., Li, C., Li, T., Wei, Z., Ma, Z., Zhang, G., Qu, C., He, H., Shan, X., 2025. Fault geometry and rupture speed as controls on off-fault deformation in the 2023 Turkey-Syria earthquakes. Commun. Earth Environ. 6, 1–13. https://doi.org/10.1038/s43247-025-02089-4.

Xie, H., Li, Z., Yuan, D., Wang, X., Su, Q., Li, X., Wang, A., Su, P., 2022. Characteristics of Co-seismic surface rupture of the 2021 Maduo Mw 7.4 earthquake and its tectonic implications for Northern Qinghai–Tibet plateau. Remote Sens. 14, 4154. https://doi.org/10.3390/rs14174154.

Xiong, W., Chen, W., Wang, D., Wen, Y., Nie, Z., Gang, L., Dijin, W., Yu, P., Qiao, X., Zhao, B., 2022. Coseismic slip and early afterslip of the 2021 Mw 7.4 Maduo, China earthquake constrained by GPS and InSAR data. Tectonophysics 840, 229558. https://doi.org/10.1016/j.tecto.2022.229558.

Yuan, Z., Li, T., Su, P., Sun, H., Ha, G., Guo, P., Chen, G., Jobe, J., 2022. Large surface-rupture gaps and low surface fault slip of the 2021 Mw 7.4 Maduo earthquake along a low-activity strike-slip fault, Tibetan plateau. Geophys. Res. Lett. 49. https://doi.org/10.1029/2021GL096874.

Zinke, R., Dolan, J., Dissen, R., Grenader, J., Rhodes, E., McGuire, C., Langridge, R., Nicol, A., Hatem, A., 2015. Evolution and progressive geomorphic manifestation of surface faulting: a comparison of the Wairau and Awatere faults, South Island, New Zealand. Geology 43, G37065. https://doi.org/10.1130/G37065.1, 1.

Zinke, R., Hollingsworth, J., Dolan, J.F., Van Dissen, R., 2019. Three-dimensional surface deformation in the 2016 MW 7.8 Kaikōura, New Zealand, earthquake from optical image correlation: implications for strain localization and long-term evolution of the Pacific-Australian plate boundary. Geochem., Geophys., Geosyst. 20, 1609–1628. https://doi.org/10.1029/2018GC007951.

Zhao, D., Qu, C., Bürgmann, R., Shan, X., 2023a. Characterizing deep, shallow, and surface fault zone deformation of the 2021 Mw 7.4 Maduo, China. Earthquake. Seismol. Res. Lett. https://doi.org/10.1785/0220230115.

Zhao, L., Xu, W., Xie, L., Zhao, D., Zhu, Z., Wu, P., Guo, H., 2023b. Fault geometry and low frictional control of the near-field postseismic deformation of the 2021 Mw 7.3 Maduo earthquake. Tectonophysics 863, 230000. https://doi.org/10.1016/j.tecto.2023.230000.